How to cite: Angew. Chem. Int. Ed. 2024, e202403771
doi.org/10.1002/anie.202403771

Nanotheranostics

Monitoring ROS Responsive Fe_3O_4-based Nanoparticle Mediated Ferroptosis&Immunotherapy via ^{129}Xe MRI

Lei Zhang[+], Maosong Qiu[+], Ruifang Wang, Sha Li, Xiaoxun Liu, Qiuyi Xu, Long Xiao, Zhong-Xing Jiang, Xin Zhou, and Shizhen Chen**

Abstract: The immune checkpoint blockade strategy has improved the survival rate of late-stage lung cancer patients. However, the low immune response rate limits the immunotherapy efficiency. Here, we report a ROS-responsive Fe_3O_4-based nanoparticle that undergoes charge reversal and disassembly in the tumor microenvironment, enhancing the uptake of Fe_3O_4 by tumor cells and triggering a more severe ferroptosis. In the tumor microenvironment, the nanoparticle rapidly disassembles and releases the loaded GOx and the immune-activating peptide Tuftsin under overexpressed H_2O_2. GOx can consume the glucose of tumor cells and generate more H_2O_2, promoting the disassembly of the nanoparticle and drug release, thereby enhancing the therapeutic effect of ferroptosis. Combined with Tuftsin, it can more effectively reverse the immune-suppressive microenvironment and promote the recruitment of effector T cells in tumor tissues. Ultimately, in combination with α-PD-L1, there is significant inhibition of the growth of lung metastases. Additionally, the hyperpolarized ^{129}Xe method has been used to evaluate the Fe_3O_4 nanoparticle-mediated immunotherapy, where the ventilation defects in lung metastases have been significantly improved with complete lung structure and function recovered. The ferroptosis-enhanced immunotherapy combined with non-radiation evaluation methodology paves a new way for designing novel theranostic agents for cancer therapy.

[*] Dr. L. Zhang,[+] Dr. M. Qiu,[+] R. Wang, Dr. S. Li, X. Liu, Q. Xu, Dr. L. Xiao, Prof. Dr. Z.-X. Jiang, Prof. Dr. X. Zhou, Prof. Dr. S. Chen
State Key Laboratory of Magnetic Resonance and Atomic and Molecular Physics, National Center for Magnetic Resonance in Wuhan, Wuhan Institute of Physics and Mathematics, Innovation Academy for Precision Measurement Science and Technology, Chinese Academy of Sciences – Wuhan National Laboratory for Optoelectronics, Wuhan 430071, P. R. China
E-mail: xinzhou@wipm.ac.cn
chenshizhen@wipm.ac.cn

Dr. L. Zhang,[+] Dr. M. Qiu,[+] R. Wang, Dr. S. Li, X. Liu, Q. Xu, Dr. L. Xiao, Prof. Dr. Z.-X. Jiang, Prof. Dr. X. Zhou, Prof. Dr. S. Chen
University of Chinese Academy of Sciences, Beijing 100049, P. R. China

Prof. Dr. X. Zhou, Prof. Dr. S. Chen
School of Biomedical Engineering, Hainan University, Haikou, Hainan 570228, P. R. China

[+] These authors contributed equally to this work

Introduction

Lung cancer is the malignant tumor with the highest global incidence and mortality rates, causing nearly a million deaths annually, with a five-year survival rate of less than 20 %.[1] Immunotherapy based on immune checkpoint blockade (ICB) strategies has brought revolutionary changes to the treatment of malignant tumors, showing certain efficacy in eradicating lung cancer.[2] However, ICB immunotherapy relies on a healthy immune system, and currently, lung cancer patients have a response rate of only 15–20 % to PD-1/PD-L1 immune checkpoint inhibitors.[3] One important reason is the immune-suppressive microenvironment of tumors. Overcoming the immune suppression microenvironment of tumor tissues, improving the efficiency of tumor antigen presentation, and enhancing immune responses are key challenges in improving the effectiveness of immunotherapy for lung cancer patients.[4] Combining PD-1/PD-L1 immune checkpoint inhibitors with other treatments designed to reverse the immune-suppressive microenvironment of tumor tissues shows great potential in increasing the effectiveness of immunotherapy for lung cancer.[5]

Ferroptosis, as an iron-dependent programmed cell death, is driven by the accumulation of reactive oxygen species, lipid peroxidation, and the downregulation of glutathione peroxidase 4 (GPX4).[6] Recent research has confirmed the excellent inhibitory effect of ferroptosis therapy on tumor growth,[7] especially in tumor cells with a high stromal phenotype that heavily depends on GPX4 to reverse lipid peroxidation for survival.[8] Importantly, ferroptosis has been identified as a form of immunogenic cell death (ICD), as tumor cells undergoing ferroptosis early on release damage-associated molecular patterns (DAMPs) to promote antigen presentation cell maturation and activation of effector T cells, resulting in infiltration in tumor tissues.[9] This has significant prospects for overcoming resistance issues in tumor treatment and enhancing immune responses in anti-tumor immunotherapy. Fe_3O_4 nanomaterials have been widely applied in tumor magnetic resonance imaging (MRI) and ferroptosis therapy,[10] possessing enhanced immunotherapeutic capabilities when combined with ICB strategies.[11] However, Fe_3O_4-mediated highly efficient ferroptosis in tumor cells remains a great challenge. The Fe_3O_4-based nanoparticle that incorporated CB-839 drugs to inhibit glutathione synthesis was developed, thereby reducing ROS quenching and improving ferroptosis therapy efficacy.[12] Apart from addressing the negative effects of GSH and increasing H_2O_2 levels, strategies to enhance the

utilization of Fe_3O_4 nanomaterials by tumor cells have been explored. Researchers have created self-aggregating Fe_3O_4 nanomaterials within tumor cells, prolonging the residence time to enhance ROS production and achieve a better ferroptosis therapy effect.[13] The scarcity of Fe_3O_4 nanomaterials reported in the literature to enhance tumor cell ferroptosis efficacy necessitates the development of new strategies for Fe_3O_4 nanomaterials to achieve a higher degree of ferroptosis therapy enhancement, combining it with immunotherapy for more efficient tumor growth suppression.

Real-time monitoring of immunotherapy for tumors through imaging methods is clinically significant for promptly understanding the effectiveness of immunotherapy and optimizing treatment plans as early as possible. For example, combining PET and CT imaging technologies can predict the expression of PD-1/PD-L1 in tumors based on differences in glucose metabolism, monitor early metabolic changes in primary tumors, and assess immune-related adverse events caused by excessive activation of the immune system, providing important value for evaluating short-term efficacy and long-term prognosis of immunotherapy.[14] However, repeated exposure of lung cancer patients to ionizing radiation significantly increases the risk of hematological tumors.[15] Additionally, optical methods are often hindered by limited penetration depth.[16]

In contrast, MRI has the advantage of non-ionizing radiation, along with high spatial resolution and good soft tissue contrast, making it widely used in clinical disease detection.[17] The mainstream MRI is based on imaging using water protons, but the lung is a cavity structure with low water proton density, severely limiting the monitoring capabilities of ^{1}H MRI in the process of lung cancer immunotherapy. Fortunately, the emerging technology of hyperpolarized ^{129}Xe MRI, with its ultra-high sensitivity, is particularly suitable for detecting lung diseases[18] and has played a crucial role in assessing lung function in COVID-19 patients.[19] It is noteworthy that the current use of ^{129}Xe MRI for real-time monitoring of lung cancer immunotherapy progress is a blank area that deserves further exploration of the value of ^{129}Xe MRI in lung cancer immunotherapy. In addition to the benefit of conducting multiple examinations within a short period, ^{129}Xe MRI offers the advantage of providing more detailed information about pulmonary microstructure and function. This includes data that cannot be obtained using traditional MRI methods.[20]

To achieve a significant ferroptosis effect on lung cancer cells, induce a stronger immune response in tumors, and thereby enhance the immunotherapeutic efficacy via ferroptosis in lung cancer, we constructed a self-supplying H_2O_2-responsive Fe_3O_4 nanoparticle loaded with glucose oxidase (GOx) and immune-activating peptide Tuftsin and modified with lipids (FGTL) (Scheme 1). When FGTL reaches the tumor region, overexpressed H_2O_2 causes the disassembly of FGTL and the release of loaded drugs. The release of loaded GOx could catalyze glucose in tumor cells to produce more H_2O_2, accelerating the Fenton reaction in the tumor region, achieving an enhanced ferroptosis effect, and promoting the activation and infiltration of T lymphocytes (CTL) in tumor tissues. Ultimately, good immunotherapeutic effects for lung metastatic cancer can be achieved. Also, the non-ionizing radiation super-sensitive ^{129}Xe MRI method was used to monitor the enhanced ferroptosis and immunotherapeutic effects on lung metastatic cancer. The results showed significant differences in lung ventilation defects and ^{129}Xe blood residence time in mice between the treatment group and the control group, indicating that this method may become a potential means for real-time monitoring of lung metastatic cancer immunotherapeutic efficacy in the future.

Results and Discussion

The preparation and characterization of FGTL nanoparticles were illustrated in Scheme 1 and Supporting Information. Firstly, the ROS-responsive Fe_3O_4 nanoparticles were prepared according to the solvothermal approach reported in the literature.[21] The spherical morphology of Fe_3O_4 nanoparticles with a homogeneous size of about 129 nm was observed from transmission electron microscopy (TEM) results (Figure 1a). With the decoration of lipids, the average hydrodynamic diameter of nanoparticles was increased from 164 nm to 202 nm and the surface of FGTL nanoparticles became smooth relatively (Figure 1b and S1). Simultaneously, the positive charge of Fe_3O_4 nanoparticles was converted to negative (Figure S2), which could reduce the uptake rate of the reticuloendothelial system (RES).[22] The ligand 3,3'-(Propane-2,2-diylbis(sulfanediyl)) dipropionic acid endows nanoparticles with the capability of ROS-responsive disassembly. The collapse behavior of FGTL nanoparticles incubated with H_2O_2 at different times was monitored by TEM. With the duration of reaction time, FGTL nanoparticles gradually collapsed into smaller Fe_3O_4 nanoparticles and formed agglomerates (Figure 1c and S4), along with the charge of FGTL nanoparticles converted from negative to positive (Figure S2), which may promote the uptake of nanoparticles by the tumor cells and thereby increase the ferroptosis efficacy. FGTL nanoparticles displayed a valid biostability, as evidenced by the size retention after incubation with PBS, 10 % fetal bovine serum-containing PBS, and DMEM environment for one week (Figure S5), respectively, facilitating drug-efficient delivery *in vivo*.

The elemental mapping of the FGTL nanoparticles confirmed the presence of O, S, and Fe elements (Figure 1d), further evidenced by the XPS analysis (Figure 1e). The characteristic peaks at 711 and 725 eV of Fe $2p_{3/2}$ and Fe $2p_{1/2}$ for Fe_3O_4 were observed and the existence of Fe^{2+} (710.2 and 723.5 eV) and Fe^{3+} (711.8 and 725.4 eV) was affirmed by the XPS analysis of FGTL nanoparticles (Figure 1f).[23] The as-prepared ROS-responsive Fe_3O_4 nanoparticles possessed the same diffraction peaks as Fe_3O_4 nanoparticles reported in the literature (Figure 1g).[24] The HRTEM image displayed the highly single-crystallinity of the Fe_3O_4 nanoparticles and the interplanar distance determined from the adjacent lattice fringes is about 0.253 nm, corresponding to [311] planes of the Fe_3O_4 single-

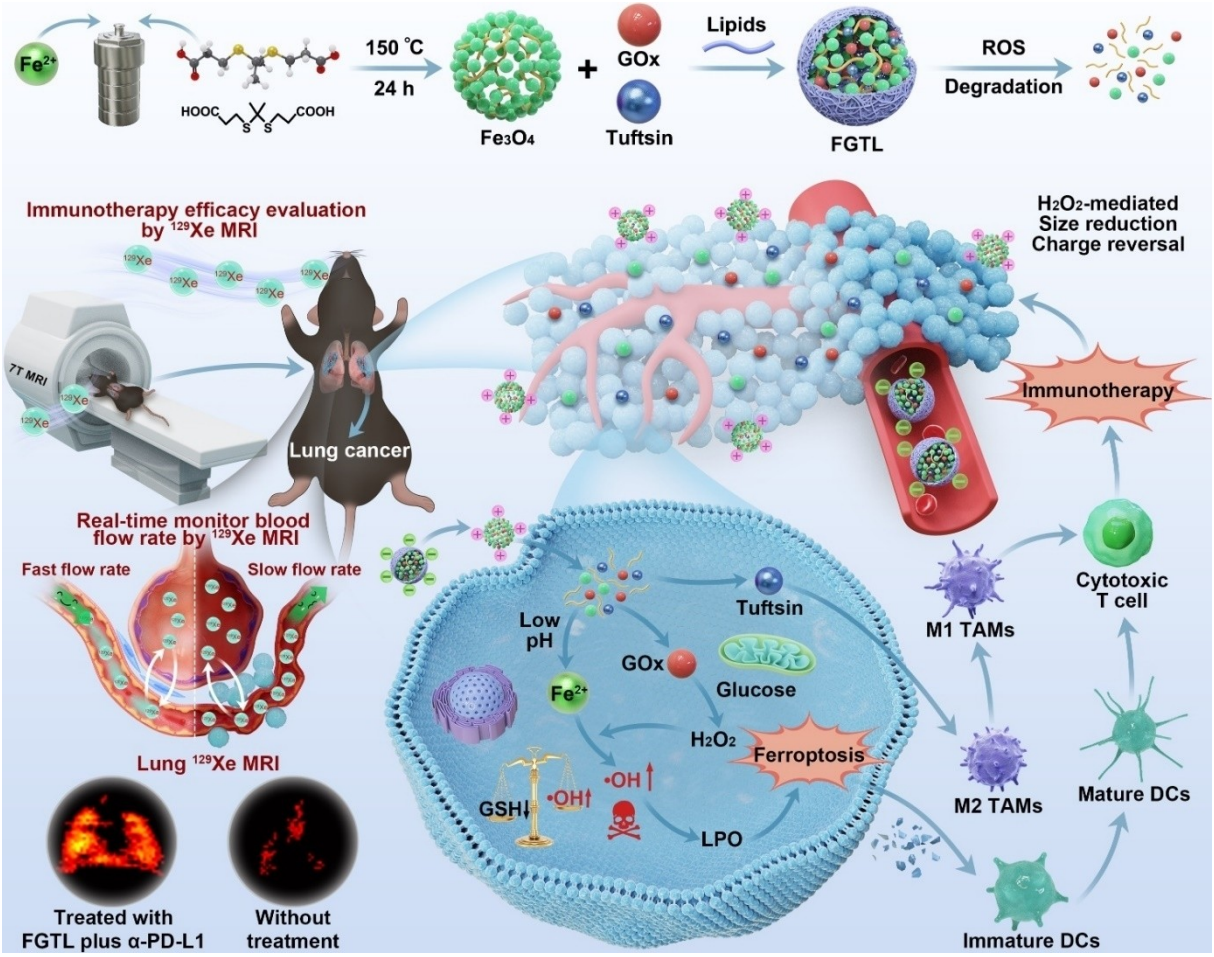

Scheme 1. Schematic illustration of the ROS-responsive FGTL-mediated ferroptosis enhanced immunotherapy of lung metastasis by reversing the immunosuppressive TME and the evaluation of immunotherapy efficacy via hyperpolarized ^{129}Xe MRI. After accumulating in the tumor region, the enhancement of ferroptosis efficiency was achieved upon the degradation of FGTL under abundant H_2O_2 conditions, reversing the immunosuppressive TME for boosting immunotherapy based on the ICB strategy. Finally, the ferroptosis-enhanced immunotherapy efficacy of lung metastasis was monitored by the ultrasensitive ^{129}Xe MRI without ionizing radiation.

crystal, which is consistent with the aforementioned XRD outcome (Figure S6).[25] The XRD characteristic peaks of ROS-responsive Fe_3O_4 nanoparticles were not changed obviously by reacting with 1 mM H_2O_2 for 4 h (Figure S7). After co-loading with GOx and immune-activating peptide Tuftsin in virtue of the presence of multi-pore in Fe_3O_4 (Figure S8) and further functionalization with lipids, the obtained Fe_3O_4@GOx@Tuftsin@Lipids (denoted as FGTL) showed an analogous morphology with the Fe_3O_4 nanoparticles (Figure 1a and 1b). The loading rates of GOx and Tuftsin were calculated to be about 9.3 % and 12.7 %, respectively (Figure S9 and S10).

The UV–vis spectrum of FGTL demonstrated that the characteristic peak intensity of GOx (276 nm) increased upon elevating H_2O_2 concentration, suggesting the ROS-responsiveness triggers the release of loaded drug (Figure 1h). With the increase of H_2O_2 concentration and the presence of glucose, the drug release rate gradually increases. Upon treatment with 1 mM H_2O_2, the release efficiency of GOx and Tuftsin in FGTL was determined as ~80.5 % and ~85.6 %, respectively, while they declined to ~15.1 % and 16.7 %, respectively. In addition, the presence of 5 mM glucose would accelerate drug release, further demonstrating the self-generation of ROS and the self-enhanced drug release capacity of FGTL nanoparticles (Figure S11 and S12). This performance can potentially conquer the limitations of incomplete drug release caused by an inadequate concentration of endogenous ROS, which could be used as a ROS-responsive drug delivery system for on-demand drug release.

Sufficient H_2O_2 in the tumor regions generated by the natural enzyme activity of GOx can be catalyzed to •OH by FGTL nanoparticles owing to the peroxidase (POD)-like nanoenzyme activity of Fe_3O_4,[26] thus enhancing the ferroptosis efficiency in tumor cells. Even if the FGTL was stored at 4 °C for 14 days, the outstanding GOx enzyme activity was maintained by monitoring the H_2O_2 production via the hydrogen peroxide Assay Kit (Figure S14). Therefore, the POD-like activity of FGTL was evaluated using methylene blue (MB) that was degraded by •OH. Not surprisingly, the

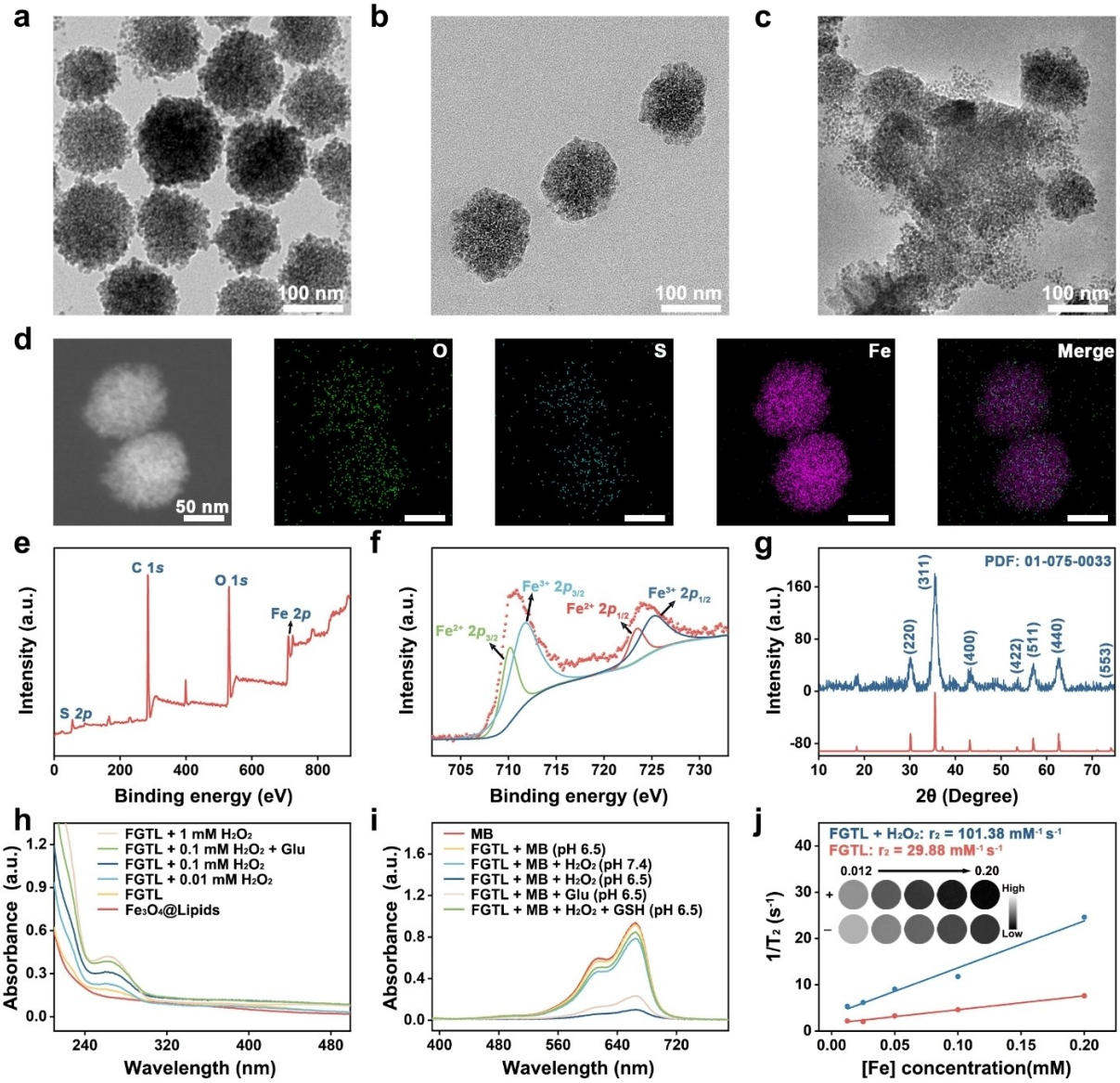

Figure 1. Characterization of the FGTL. (a-c) TEM images of (a) Fe_3O_4, (b) FGTL, and (c) FGTL treated with 1 mM H_2O_2 for 4 h. (d) STEM and elemental mapping of FGTL. (e) XPS spectrum and (f) Fe2*p* XPS analysis of Fe_3O_4. (g) XRD spectra of Fe_3O_4. (h) The UV–vis absorption spectra of Fe_3O_4@Lipids and FGTL treated with H_2O_2 (Glu: glucose). (i) The UV–vis absorption spectra of MB treated with FGTL under various conditions. (j) ^1H T_2-weighted MRI of various concentrations of FGTL with or without treatment of 1 mM H_2O_2 and the corresponding r_2 values.

FGTL combined MB exhibited similar UV–vis–NIR absorption with free MB solution. Upon exposure to the H_2O_2, the obvious attenuation of UV–vis–NIR absorption intensity of MB was observed in the FGTL plus 1 mM H_2O_2 (pH 6.5) and FGTL plus glucose (5 mM) groups, indicating the generation of •OH via the FGTL-mediated Fenton-like reaction (Figure 1i). The produced •OH was further authenticated by the ESR technique with a featured spectrum of 1:2:2:1 (Figure S15).[27] Notably, the ignorable reduction of MB UV–vis–NIR absorption was observed after treatment with FGTL plus 1 mM H_2O_2 (pH 7.4), suggesting the biosafety of *in vivo* application.

Next, the MRI experiments of FGTL were performed. The T_1-weighted MRI of FGTL with various concentrations treated with H_2O_2 or not showed implicit signal changes and relatively low longitudinal relaxivity (r_1) values (0.68 and 0.23 $mM^{-1}s^{-1}$) (Figure S17),[28] denying its application in ^1H T_1 contrast agent. In contrast, the ^1H T_2-weighted MRI signals of those samples exhibited significant enhancement with increasing concentration. The corresponding transverse relaxivity (r_2) values of FGTL and FGTL + H_2O_2 were determined as 29.88 $mM^{-1}s^{-1}$ and 101.38 $mM^{-1}s^{-1}$ (Figure 1j), respectively, suggesting the great potential application of FGTL in cancer diagnosis.

Based on the •OH-generating capacity of FGTL, the ferroptosis efficacy of LLC cells was first evaluated. Confocal laser scanning microscope (CLSM) images and flow cytometry (FCM) analysis of LLC cells incubated with

FITC-labelled FGTL (FITC@FGTL) revealed the successful endocytosis of FITC@FGTL (Figure S18). Moreover, the decoration of lipids endows FGTL with the ability of low phagocytosis by macrophages for further advancement to *in vivo* applications (Figure S19). To determine the tumor penetration capacity of FGTL, the CLSM images of LLC cell-based multicellular spheroids (MCSs) were performed. As expected, the MCSs incubated with FITC@FGTL exhibited relatively stronger fluorescence intensity and deeper penetration based on the 2D and 3D images compared with those treated with FITC@FTL (without GOx). This was attributed to the H_2O_2 generating capacity of FGTL, leading to the collapse and the charge conversion of FGTL. Moreover, the enhanced infiltration of FGTL post-treatment with additional H_2O_2 (1 mM) was achieved, as indicated via the conspicuous green fluorescence extensively dispersed over the whole MCSs (Figure S20). These results collectively suggested that the FGTL is a promising nanoparticle for overcoming the biobarriers and enhancing drug delivery efficiency by H_2O_2-mediated size reduction and charge conversion of FGTL in the tumor region, pursuing the high-efficiency ferroptosis of tumor cells.

To evaluate the FGTL-mediated ferroptosis efficiency at the cellular level, the generation of intracellular ROS (indicated by DCFH-DA) and lipid peroxidation (indicated by BODIPY–C11) were determined by CLSM after various treatments. The cellular ROS level was elevated in FGTL-treated LLC cells compared with other groups. Notably, the introduction of ferrostatin-1 (Fer-1) significantly downregulated the cellular ROS level in FGTL-treated cells (Figure 2a and 2d), indicating ferroptosis occurred in FGTL-treated cells. Moreover, the cellular lipid peroxidation level, one critical characteristic in ferroptosis, displayed a similar tendency of change with ROS, further verifying the excellent FGTL-mediated ferroptosis of LLC cells (Figure 2b and 2d). Mitochondrial dysfunction is one of the key indicators of ferroptosis, thus the mitochondrial membrane potential (MMP) was measured by using fluorescence probe JC-1, which fluoresces red in intact mitochondria or green in depolarised mitochondria. As expected, a significant MMP loss was observed in the FGTL-treated group that displayed apparent green fluorescence in LLC cells (Figure 2c and 2d). For the visualization of mitochondrial shrinkage in tumor cells, the TEM experiments of LLC cells treated with FGTL and PBS were carried out, respectively. Compared with the PBS group, FGTL-treated LLC cells exhibited obvious mitochondrial damage characterized by smaller mitochondria, the disappearance of mitochondrial cristae, rupture of the outer mitochondrial membrane, and condensed mitochondrial membrane densities (Figure 2e).[29] Glutathione peroxidase 4 (GPX4) plays a dominant role in blocking ferroptosis by catalyzing the reduction of lipid peroxides.[30] Therefore, the western blot experiments were performed to evaluate the GPX4 expression. The western blot results showed that the level of GPX4 expression in LLC cells was significantly down-regulated upon treatment with FGTL compared with those treated with PBS, GOx, and Fe_3O_4@Tuftsin@Lips (denoted as FTL). Notably, this down-regulation was reversed upon the addition of Fer-1, illustrating the FGTL-treated LLC cells were involved in ferroptosis (Figure 2f). These outcomes collectively demonstrated FGTL-mediated enhancement of LLC cell ferroptosis by self-generating H_2O_2-catalyzed •OH generation.

Subsequently, the *in vitro* FGTL-mediated ferroptosis therapeutic efficacy of tumor cells was evaluated by the CCK8 assay and the live/dead cell staining with Calcein-AM/PI. The cytotoxicity of 4T1 cells, A549 cells, B16F10 cells, and LLC cells was significantly elevated along with the FGTL-incubated concentration increased, while the low cytotoxicity of MRC-5 cells was found (Figure S22). Upon treatment with Fer-1, the tumor cell viability was improved (Figure 2g). The intracellular green fluorescence (indicating live cells) was dominant in the PBS, GOx, and FTL treatment groups. In contrast, the distinct red fluorescence (indicating dead cells) was observed in FGTL-treated LLC cells, while it was inversed by the addition of Fer-1 (Figure S23). In addition, the FCM of Annexin V-FITC/PI staining in LLC cells was performed for the further quantification of the *in vitro* FGTL-induced ferroptosis therapeutic efficacy. The cell necrosis rates in PBS, GOx, FTL, FGTL, and FGTL plus Fer-1 groups were 6.7 %, 19.1 %, 40.0 %, 81.5 %, and 21.0 %, respectively, further confirming the accuracy of CCK8 and CSLM results (Figure 2h). The cellular therapeutic efficacy outcomes indicated that FGTL-induced enhancement of ferroptosis was achieved, possessing great promise for the inhibition of lung cancer growth *in vivo*.

Fe_3O_4-based nanoparticles with effective tumor region accumulation can benefit the enhancement of ferroptosis. FGTL achieved an exceptional dual-modal imaging capability in both MR and fluorescence by incorporating IR820 (referred to as FGITL) (Figure 1j, S24, and S25). To assess the *in vivo* enrichment of FGTL in the tumor region, the subcutaneous LLC tumor-bearing mice model was first performed for the whole body fluorescence imaging (FLI). The fluorescence signal intensity of the tumor region increased gradually and reached a peak at 24 h post-injection of FGITL (Figure S27a and S27c). The *ex vivo* FLI of isolated tumor and main tissues including the heart, liver, spleen, lung, and kidneys obtained at 36 h post-injection revealed that the fluorescence signal of the tumor was 1.4- and 2.0-fold higher than that of the liver and kidneys, indicating the high-efficiency enrichment of FGITL in the tumor region (Figure S27d and S28). Moreover, the ^1H T_2-weighted MRI of subcutaneous LLC tumor-bearing mice was performed. Similar to FLI, the tumor/muscle MR contrast at 12 h post-injection enhanced by 14.1 % compared with that of 0 h (Figure S27b and S27e). The above results of fluorescence/MR dual-modal imaging confirmed that FGTL was equipped with effective tumor accumulation capability, guaranteeing the high-efficiency ferroptosis of tumor cells.

The immunogenic cell death of tumor cells can be achieved by the nanoparticles-induced ferroptosis of tumor cells, ultimately activating local immune responses in tumors.[31] The M2 macrophages are the dominant phenotype in the immunosuppressive TME. Reversing the immunosuppressive TME by promoting the M2-to-M1 phenotype switch is a practicable strategy. Thus, the RAW264.7 macro-

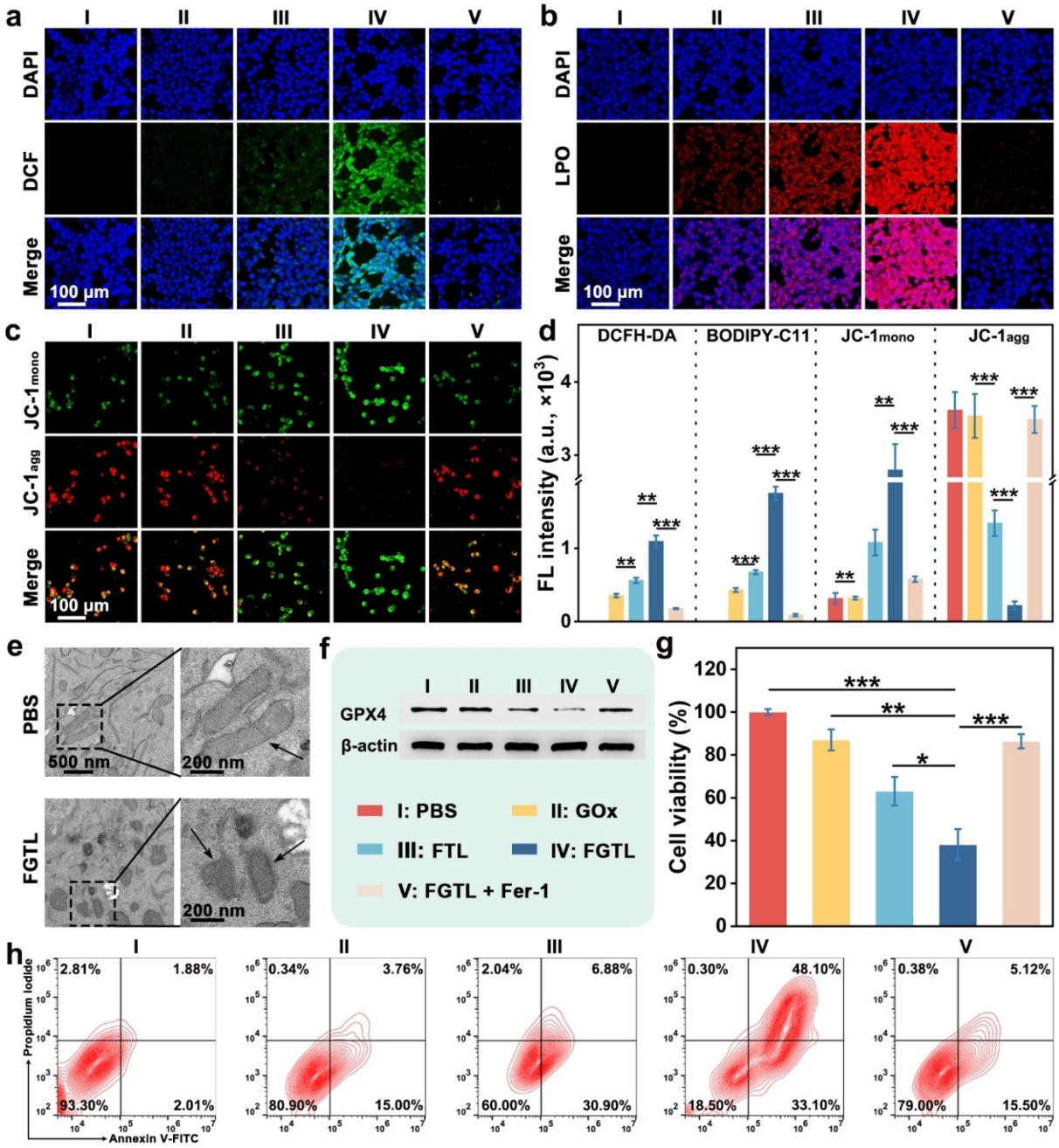

Figure 2. *In vitro* mechanism of ferroptosis and cytotoxicity induced by FGTL. (a-c) CLSM images of LLC cells staining with (a) DCFH-DA (indicated FGTL-induced ROS generation), (b) BODIPY–C11 (indicated FGTL-induced lipid peroxidation), and (c) JC-1 (JC-1_{mono} and JC-1_{agg} fluorescent images showing mitochondria membrane potential ($\Delta\psi_m$) after different treatments and (d) the corresponding fluorescence intensity analysis (mean ± SD, $n = 3$, $^{**}p < 0.01$, $^{***}p < 0.001$). (e) The TEM images of LLC cells treated with PBS and FGTL, respectively. (f) The western blotting analysis of LLC cells and (g) cell viability of LLC cells after different treatments. (mean ± SD, $n = 3$, $^{*}p < 0.05$, $^{**}p < 0.01$, $^{***}p < 0.001$). (h) Flow cytometry quantification of LLC cell apoptosis after various treatments.

phages were cocultured with residues of LLC cells treated with PBS, FGL, or FGTL in a transwell chamber system. The corresponding proportion of M2 and M1 phenotype macrophages was determined by the FCM after staining with anti-F4/80, anti-CD86, and anti-CD206 antibodies (Figure S29). Compared with the PBS group, the proportion of M2 macrophages ($CD206^+CD86^-$) in the FGL and FGTL groups declined obviously from 49.0 % to 35.4 % and 23.8 %, respectively. Simultaneously, the proportion of M1 macrophages ($CD206^-CD86^+$) elevated significantly from 44.0 % to 53.3 % and 65.8 %, respectively (Figure S30), confirming the preeminent performance of FGTL-mediated M1 macrophage polarization and the further promoted polarization by the loading of Tuftsin.

Encouraged by the appreciable amelioration of immunosuppressive TME at the cellular level, the immune-related

cells including macrophages, dendritic cells (DCs), and T cells in the tumor region were analyzed by using subcutaneous LLC tumor-bearing mice. The tumors were harvested after *i. v.* injection of PBS, FGL, and FGTL for 7 days. Upon digesting into a single-cell suspension and staining with commercial antibodies, the infiltration of immune cells was evaluated by FCM ($n=3$) (Figure 3a). The correspondingly immune cells in FCM results were acquired through a gating strategy (Figure S31 and S32). Encouragingly, both the changing tendency of M2 (decreased from 49.0 % to 35.4 % and 23.8 %) and M1 (increased from 49.0 % to 35.4 % and 23.8 %) phenotype macrophages were similar to the cellular outcomes after treatment with PBS, FGL, and FGTL, demonstrating that FGTL-mediated ferroptosis was beneficial for the occurrence of inflammation in the tumor area (Figure 3b and 3g). The exposure of tumor-associated antigens could promote DCs maturation.[32] Compared with the PBS group, the proportion of DCs maturation ($CD80^+CD86^+$) in the tumor significantly increased from 49.30 % to 67.20 %, and 82.40 % (Figure 3c and 3g). Beyond that, the DCs maturation could accelerate the infiltration of cytotoxic T lymphocytes, enhancing the immunotherapy efficiency based on ICB

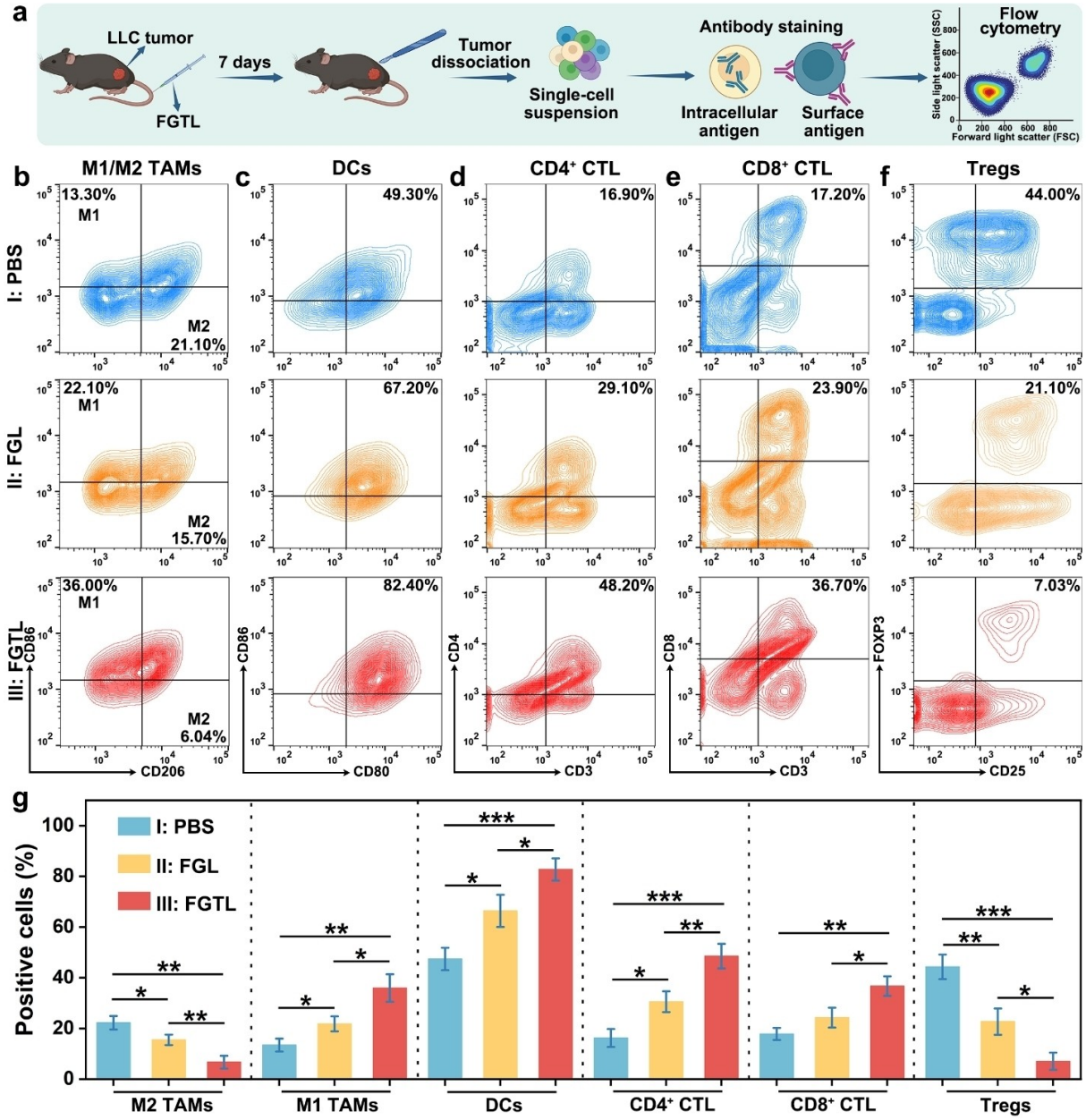

Figure 3. *In vivo* immune activated by FGTL. (a) Schedule for determination of *in vivo* immune-activated performances of FGTL by FCM quantitation analysis of macrophages, DCs, and T cells in the tumor. (b-f) Representative FCM plots and (g) the corresponding quantitative analysis on the proportion of tumor-infiltrating M2 phenotype and M1 phenotype macrophages, mature dendritic cells, $CD4^+$ CTL, $CD8^+$ CTL, and Treg cells in the LLC tumor-bearing mice post *i. v.* injection of FGTL for 7 days (mean ± SD, $n=3$, $^*p<0.05$, $^{**}p<0.01$, and $^{***}p<0.001$)

strategies. As expected, the $CD3^+CD4^+$ and $CD3^+CD8^+$ T cells (16.9 % and 17.2 %) in the PBS group were substantially improved in the FGL (29.1 % and 23.9 %) and FGTL (48.2 % and 36.7 %) groups (Figure 3d, 3e, and 3g). In addition, abundant regulatory T (Treg) cells ($CD25^+FOXP3^+$) that play a negative immune regulatory role in the PBS group (44.0 %) were observed, while it was down-regulated to 21.1 % and 7.0 % in the FGL and FGTL groups (Figure 3f and 3g). Collectively, these outcomes indicated that FGTL-mediated ferroptosis of tumor cells could effectively reverse immunosuppressive TME to favorable anti-tumor immunities by improving the proportion of M1 macrophages, DCs, $CD4^+$, and $CD8^+$ T cells and reducing the proportion of M2 macrophages and Treg cells.

Invigorated by the FGTL-mediated high-efficiency ferroptosis-activated tumor local immune response, the subcutaneous LLC tumor-bearing mice were applied to evaluate the *in vivo* ferroptosis anti-tumor efficiency synergy with ICB-based immunotherapy by α-PD-L1. The blood glucose in FGTL-treated mice did not display a continuous decrease compared with the pre-injection (Figure S33a), proving the preeminent blood safety of FGTL. Due to the explosive growth pattern of LLC cells, the various treatments (I: PBS, II: α-PD-L1, III: FTL, IV: FGTL, V: FGTL + α-PD-L1) of mice were performed on day 3 after being subcutaneously injected with LLC cells on the leg (Figure S33b). Compared to the I–III groups with a 31.3-fold, 31.6-fold, and 22.6-fold relative tumor volume on day 14, respectively, FGTL (12.4-fold) treatment revealed medium anti-tumor efficiency. Significantly, the FGTL + α-PD-L1 treatment group with a 3.9-fold relative tumor volume showed prominent and potent anti-tumor efficiency by FGTL-induced ferroptosis-enhanced immunotherapy (Figure S33c). The tumor growth inhibition rates of group II–V were 2.4 %, 30.8 %, 62.3 %, and 88.2 % (Figure S34). The photograph of the tumor harvested on day 14 and the relative tumor weight of groups I–IV (9.9-fold, 7.4-fold, 6.2-fold, and 3.2-fold compared to group V) confirmed the strongest therapeutic efficiency in the synergy therapy group of ferroptosis&ICB immunotherapy (Figure S33d and S33e).

To evaluate the anti-tumor effect at the cellular level, the tumor sections were imaged after H&E, TUNEL, and Ki-67 straining, respectively. Reasonably, all of the tumor slice images in the FGTL + α-PD-L1 group showed the most severe damage to tumor cells (Figure S33f). For a better understanding of the mechanism of ferroptosis-enhanced immunotherapy, the tumor slices were strained by the ROS staining solution, HMGB1, CD206/CD86, and CD4/CD8 antibodies. The ROS staining results displayed the most eye-catching red fluorescence in the FGTL + α-PD-L1 group, leading to the serious immunogenic death of tumor cells characterized by the remarkable HMGB1 protein expression level. Ultimately, the immunosuppressive TME was reversed as demonstrated by the up-regulation of M1 macrophage, down-regulation of M2 macrophage, and the infiltration of abundant $CD4^+$ and $CD8^+$ T cells in the tumor, achieving the FGTL-induced enhancement of ferroptosis&immunotherapy therapeutic efficacy (Figure S35). Throughout the therapy period, the body weight of mice in all groups was kept at a balanced level (Figure S36). The results of H&E staining of main organs and blood biochemical analysis reveal the good biosafety of FGTL (Figure S37).

Furthermore, a lung metastasis model was established to assess the inhibitory effect of FGTL (Figure 4a). Exceeding the expected inhibitory effect was observed in the mice injected with FGTL and α-PD-L1, as evidenced by the smallest number and volume of pulmonary nodules shown in the CT images and anatomical photographs of the lungs compared to the other groups (Figure 4b and 4c). Both the H&E staining and weight analysis of the isolated lungs further authenticate the aforementioned results (Figure 4d and S38). In groups I–II with severe lung metastasis, the mice gradually weakened and showed a trend of body weight loss (Figure S39). Meanwhile, mice treated with FGTL and α-PD-L1 displayed a noticeable prolonged survival time compared to groups I–III (Figure S40). In addition, the proportion of the effector memory T cells (T_{EM}, $CD62L^-CD44^+$) at day 22 was conspicuously elevated in group IV, while the proportion of central memory T cells (T_{CM}, $CD62L^+CD44^+$) diminished correspondingly (Figure 4e and 4f), suggesting the long-term immune response effect. All of the above outcomes confirmed that FGTL nanoplatform could inhibit lung cancer metastasis by the united superiority of the enhancement of ferroptosis via the H_2O_2-mediated size reduction and charge conversion of FGTL, FGTL-induced reversion of tumor immunosuppressive microenvironment and α-PD-L1-blockade immune escape suppression.

Real-time monitoring of immunotherapy therapeutic efficacy accelerates understanding of the therapeutic schedule and cancer progression, which is crucial to the timely optimization of the therapy strategy. Radiation-based diagnosis protocols including PET and CT imaging are extensively used for the diagnosis of lung diseases, but they are not suitable for multiple lung scans in a short period due to the radiation exposure. In virtue of the non-ionizing radiation and high sensitivity of hyperpolarized ^{129}Xe MRI, the lung ^{129}Xe ventilation image and gas exchange efficiency in the blood plasma of the lung can be obtained,[33] providing information on lung structure and function concurrently. To evaluate the immunotherapy efficacy in real-time, the ^{129}Xe ventilation MRI and chemical shift saturation recovery (CSSR) experiments of the lung were performed. Conspicuously, the ^{129}Xe ventilation MRI exhibited a complete shape of the lung in the FGTL plus α-PD-L1 group and healthy mice while obvious ventilation deficiency was observed in the other groups (Figure 5a and S41), attributed to the occupation of lung metastatic cancer cells in the lungs. This was authenticated by the images and H&E staining of the isolated lung (Figure 5b), further illustrating the reliability of FGTL-mediated ferroptosis-enhanced immunotherapy efficacy. To gain a better understanding of the therapeutic efficacy of lung metastasis from an in-depth perspective, the ^{129}Xe transit time of blood (Tau), alveolar septal thickness (d), and the ratio of the alveolar septal volume relative to the gas space volume (Vs/Va) of the lung in various treatment groups were determined by the analysis of the

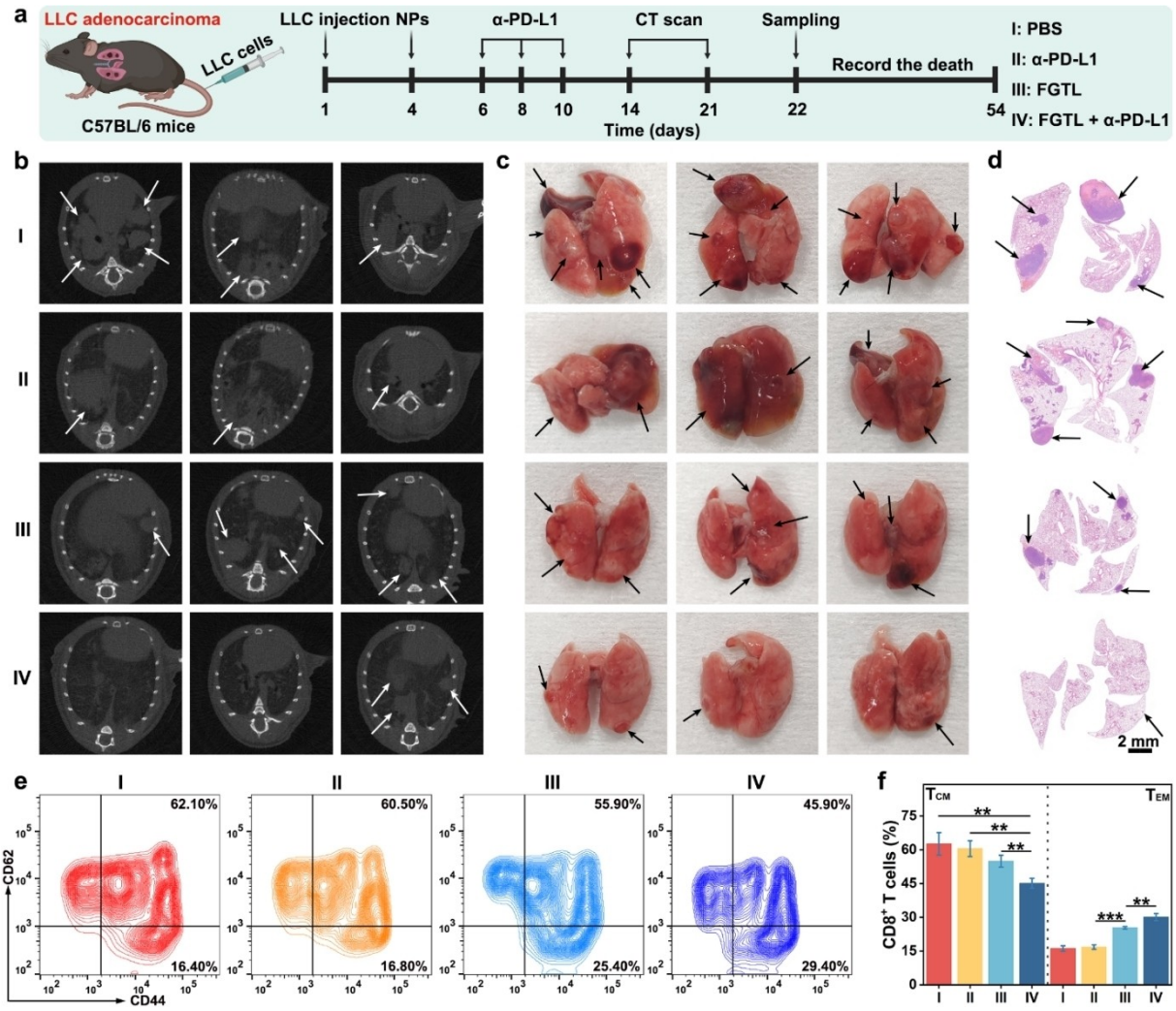

Figure 4. *In vivo* FGTL-mediated ferroptosis enhanced immunotherapy of lung metastasis. (a) Schematic illustration of LLC cells metastasis therapeutic schedule. (b) CT images, (c) Photographs, and (d) H&E straining of the lung in various treatment groups. (e) Representative FCM plots and (f) the corresponding quantitative analysis on the proportion of T_{CM} and T_{EM} cells in the spleen at day 22 (mean ± SD, $n = 3$, $^{**}p < 0.01$, $^{***}p < 0.001$).

CSSR spectrum. Significantly, the value of Tau in the FGTL plus α-PD-L1 group was much lower than that of the other group (Figure 5c). This may be caused by the faster blood flow rate in group IV due to less compression from tumor cells compared to groups I–III. Furthermore, the values of d and Vs/Va among I–IV groups showed a downward trend (Figure 5d and 5e), which may be attributed to the volume of alveoli decreasing with the increase of tumor cells in lung tissue. These results revealed that the immunotherapy efficacy of lung metastasis could be precisely evaluated by the ^{129}Xe MRI, which could be used as a non-invasive imaging technology for medication guidance in immunotherapy.

Conclusion

In conclusion, we have constructed a self-supplying H_2O_2-responsive Fe_3O_4-based nanoparticle. In the overexpressed H_2O_2 environment of tumor tissues, the nanoparticle can undergo disassembly, causing the surface charge to change from negative to positive and reducing the nanoparticle size. Both of these factors promote the uptake rate of the nanoparticles by tumor cells and enhance the deep delivery of nanoparticles into tumor tissue. In addition, the disintegration of nanoparticles further releases loaded GOx, catalyzing the production of more H_2O_2 within tumor cells. This ultimately leads to more severe lipid peroxidation in tumor cells, enhancing the therapeutic effect of ferroptosis in tumor cells. The more efficient ferroptosis achieved through nanoparticle disassembly can generate more tumor cell fragments, which, as antigens, can stimulate DCs maturation and activation of cytotoxic T cells, as well as infiltration into tumor tissues, thereby more effectively activating the immune response of tumor tissues. Finally, in combination with α-PD-L1, more efficient immunotherapeutic effects for lung metastatic cancer were achieved. It is worth mentioning that using the advantages of hyperpolar-

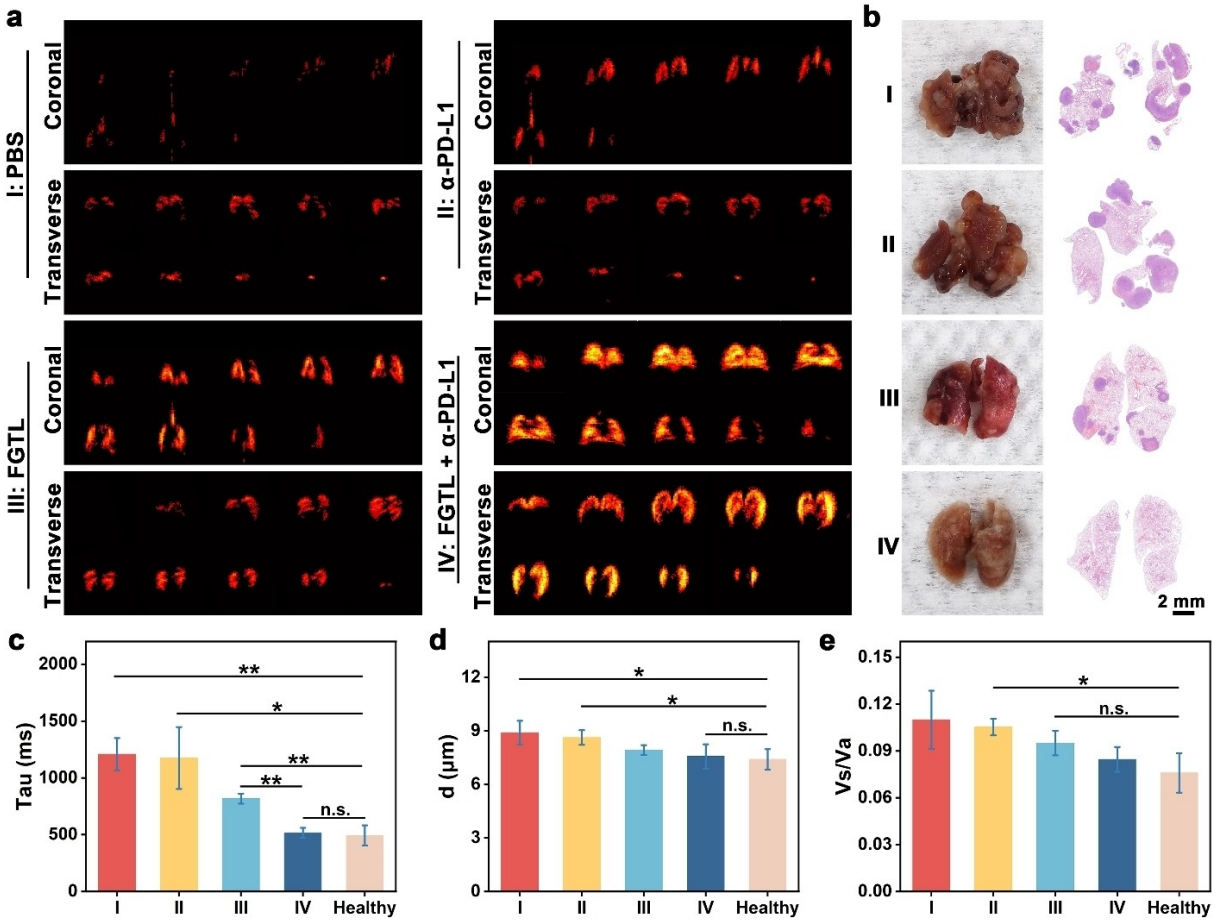

Figure 5. The assessment of FGTL-mediated ferroptosis enhanced immunotherapy of lung metastasis by ^{129}Xe MRI. (a) The representative coronal and transverse ^{129}Xe ventilation MRI and (b) the corresponding photos and H&E staining of the lung in various treatment groups. (c) The ^{129}Xe transit time of blood (T_{au}), (d) alveolar septal thickness (d), and (e) the ratio of the alveolar septal volume relative to the gas space volume (V_s/V_a) of the lung in various treatment groups calculated by the CSSR method (mean ± SD, $n = 5$, n.s.: no significance, *$p < 0.05$, **$p < 0.01$).

ized ^{129}Xe MRI, which is super-sensitive and non-ionizing radiation, for the effective evaluation of immunotherapeutic effects in lung metastatic cancer, significant differences in lung ventilation defects and the blood residency time of ^{129}Xe can be observed. This represents an emerging means of evaluating lung cancer treatment. This strategy for the treatment and efficacy evaluation of lung metastatic cancer has important prospects for potential future clinical applications.

Acknowledgements

This work was funded by the National Key R&D Program of China (2018YFA0704000), the National Natural Science Foundation of China (U21A20392, 82127802, 21921004, and 81901737), the Hubei Provincial Natural Science Foundation of China (grant no. 05182321), and the CAS Youth Interdisciplinary Team (JCTD-2022-13). Xin Zhou acknowledges the support from the Tencent Foundation through the XPLORER PRIZE, and Shizhen Chen acknowledges the support from the Young Top-notch Talent Cultivation Program of Hubei Province.

Conflict of Interest

The authors declare no conflict of interest.

Data Availability Statement

The data that support the findings of this study are available from the corresponding author upon reasonable request.

Keywords: MRI · hyperpolarized ^{129}Xe · Fe_3O_4 · ferroptosis · immunotherapy

[1] a) R. L. Siegel, K. D. Miller, N. S. Wagle, A. Jemal, *Ca-Cancer J. Clin.* **2023**, *73*, 17–48; b) X. Zheng, X. Song, G. Zhu, D. Pan, H. Li, J. Hu, K. Xiao, Q. Gong, Z. Gu, K. Luo, W. Li, *Adv. Mater.* **2024**, *36*, e2308977; c) H. Wakelee, M. Liberman, T.

Kato, M. Tsuboi, S. H. Lee, S. Gao, K. N. Chen, C. Dooms, M. Majem, E. Eigendorff, G. L. Martinengo, O. Bylicki, D. Rodríguez-Abreu, J. E. Chaft, S. Novello, J. Yang, S. M. Keller, A. Samkari, J. D. Spicer, *N. Engl. J. Med.* **2023**, *389*, 491–503.

[2] L. Liu, Y. Pan, C. Zhao, P. Huang, X. Chen, L. Rao, *ACS Nano* **2023**, *17*, 3225–3258.

[3] M. Reda, W. Ngamcherdtrakul, M. A. Nelson, N. Siriwon, R. Wang, H. Y. Zaidan, D. S. Bejan, S. Reda, N. H. Hoang, N. A. Crumrine, J. P. C. Rehwaldt, A. Bindal, G. B. Mills, J. W. Gray, W. Yantasee, *Nat. Commun.* **2022**, *13*, 4261.

[4] a) A. Lahiri, A. Maji, P. D. Potdar, N. Singh, P. Parikh, B. Bisht, A. Mukherjee, M. K. Paul, *Mol. Cancer* **2023**, *22*, 40; b) L. Liu, J. Zhang, R. An, Q. Xue, X. Cheng, Y. Hu, Z. Huang, L. Wu, W. Zeng, Y. Miao, J. Li, Y. Zhou, H. Y. Chen, H. Liu, D. Ye, *Angew. Chem. Int. Ed.* **2023**, *62*, e202217055.

[5] a) H. Li, Q. Luo, H. Zhang, X. Ma, Z. Gu, Q. Gong, K. Luo, *Chem. Soc. Rev.* **2023**, *52*, 47–96; b) J. Meng, X. Yang, J. Huang, Z. Tuo, Y. Hu, Z. Liao, Y. Tian, S. Deng, Y. Deng, Z. Zhou, J. F. Lovell, H. Jin, Y. Liu, K. Yang, *Adv. Sci.* **2023**, *10*, e2300517; c) C. Xu, J. Huang, Y. Jiang, S. He, C. Zhang, K. Pu, *Nat. Biomed. Eng.* **2023**, *7*, 298–312; d) J. Yu, S. He, C. Zhang, C. Xu, J. Huang, M. Xu, K. Pu, *Angew. Chem. Int. Ed.* **2023**, *62*, e202307272.

[6] A. N. von Krusenstiern, R. N. Robson, N. Qian, B. Qiu, F. Hu, E. Reznik, N. Smith, F. Zandkarimi, V. M. Estes, M. Dupont, T. Hirschhorn, M. S. Shchepinov, W. Min, K. A. Woerpel, B. R. Stockwell, *Nat. Chem. Biol.* **2023**, *19*, 719–730.

[7] a) X. Fang, H. Ardehali, J. Min, F. Wang, *Nat. Rev. Cardiol.* **2023**, *20*, 7–23; b) L. Xie, J. Li, G. Wang, W. Sang, M. Xu, W. Li, J. Yan, B. Li, Z. Zhang, Q. Zhao, Z. Yuan, Q. Fan, Y. Dai, *J. Am. Chem. Soc.* **2022**, *144*, 787–797.

[8] a) V. S. Viswanathan, M. J. Ryan, H. D. Dhruv, S. Gill, O. M. Eichhoff, B. Seashore-Ludlow, S. D. Kaffenberger, J. K. Eaton, K. Shimada, A. J. Aguirre, S. R. Viswanathan, S. Chattopadhyay, P. Tamayo, W. S. Yang, M. G. Rees, S. Chen, Z. V. Boskovic, S. Javaid, C. Huang, X. Wu, Y. Y. Tseng, E. M. Roider, D. Gao, J. M. Cleary, B. M. Wolpin, J. P. Mesirov, D. A. Haber, J. A. Engelman, J. S. Boehm, J. D. Kotz, C. S. Hon, Y. Chen, W. C. Hahn, M. P. Levesque, J. G. Doench, M. E. Berens, A. F. Shamji, P. A. Clemons, B. R. Stockwell, S. L. Schreiber, *Nature* **2017**, *547*, 453–457; b) M. J. Hangauer, V. S. Viswanathan, M. J. Ryan, D. Bole, J. K. Eaton, A. Matov, J. Galeas, H. D. Dhruv, M. E. Berens, S. L. Schreiber, F. McCormick, M. T. McManus, *Nature* **2017**, *551*, 247–250.

[9] a) Z. Li, L. Rong, *Biomater. Sci.* **2020**, *8*, 6272–6285; b) L. Zhang, A. Song, Q. C. Yang, S. J. Li, S. Wang, S. C. Wan, J. Sun, R. T. K. Kwok, J. W. Y. Lam, H. Deng, B. Z. Tang, Z. J. Sun, *Nat. Commun.* **2023**, *14*, 5355.

[10] Y. Wang, X. Wu, X. Bao, X. Mou, *Molecules* **2023**, *28*, 4562.

[11] a) I. Efimova, E. Catanzaro, L. Van der Meeren, V. D. Turubanova, H. Hammad, T. A. Mishchenko, M. V. Vedunova, C. Fimognari, C. Bachert, F. Coppieters, S. Lefever, A. G. Skirtach, O. Krysko, D. V. Krysko, *J. Immunother. Cancer* **2020**, *8*, e001369; b) W. Wang, M. Green, J. E. Choi, M. Gijón, P. D. Kennedy, J. K. Johnson, P. Liao, X. Lang, I. Kryczek, A. Sell, H. Xia, J. Zhou, G. Li, J. Li, W. Li, S. Wei, L. Vatan, H. Zhang, W. Szeliga, W. Gu, R. Liu, T. S. Lawrence, C. Lamb, Y. Tanno, M. Cieslik, E. Stone, G. Georgiou, T. A. Chan, A. Chinnaiyan, W. Zou, *Nature* **2019**, *569*, 270–274.

[12] F. Wu, Y. Du, J. Yang, B. Shao, Z. Mi, Y. Yao, Y. Cui, F. He, Y. Zhang, P. Yang, *ACS Nano* **2022**, *16*, 3647–3663.

[13] Z. Zhang, B. Xie, X. Lu, L. Xiong, X. Li, Y. Zhang, C. Li, C. Wang, *Nanoscale* **2024**, *16*, 903–912.

[14] a) H. Y. Seol, Y. S. Kim, S. J. Kim, *Thorac. Cancer* **2020**, *11*, 3260–3268; b) C. H. Chang, J. Qiu, D. O'Sullivan, M. D. Buck, T. Noguchi, J. D. Curtis, Q. Chen, M. Gindin, M. M. Gubin, G. J. van der Windt, E. Tonc, R. D. Schreiber, E. J. Pearce, E. L. Pearce, *Cell* **2015**, *162*, 1229–1241; c) M. Z. Noman, G. Desantis, B. Janji, M. Hasmim, S. Karray, P. Dessen, V. Bronte, S. Chouaib, *J. Exp. Med.* **2014**, *211*, 781–790; d) N. Aide, R. J. Hicks, C. Le Tourneau, S. Lheureux, S. Fanti, E. Lopci, *Eur. J. Nucl. Med. Mol. Imaging* **2019**, *46*, 238–250.

[15] M. Bosch de Basea Gomez, I. Thierry-Chef, R. Harbron, M. Hauptmann, G. Byrnes, M. O. Bernier, L. Le Cornet, J. Dabin, G. Ferro, T. S. Istad, A. Jahnen, C. Lee, C. Maccia, F. Malchair, H. Olerud, S. L. Simon, J. Figuerola, A. Peiro, H. Engels, C. Johansen, M. Blettner, M. Kaijser, K. Kjaerheim, A. Berrington de Gonzalez, N. Journy, J. M. Meulepas, M. Moissonnier, A. Nordenskjold, R. Pokora, C. Ronckers, J. Schüz, A. Kesminiene, E. Cardis, *Nat. Med.* **2023**, *29*, 3111–3119.

[16] a) G. Guan, C. Zhang, H. Liu, Y. Wang, Z. Dong, C. Lu, B. Nan, R. Yue, X. Yin, X. B. Zhang, G. Song, *Angew. Chem. Int. Ed.* **2022**, *61*, e202117229; b) Z. Dong, P. Liang, G. Guan, B. Yin, Y. Wang, R. Yue, X. Zhang, G. Song, *Angew. Chem. Int. Ed.* **2022**, *61*, e202206074; c) R. Yue, C. Zhang, L. Xu, Y. Wang, G. Guan, L. Lei, X. Zhang, G. Song, *Chem* **2022**, *8*, 1956–1981.

[17] a) S. Chen, L. Xiao, Y. Li, M. Qiu, Y. Yuan, R. Zhou, C. Li, L. Zhang, Z. X. Jiang, M. Liu, X. Zhou, *Angew. Chem. Int. Ed.* **2022**, *61*, e202213495; b) S. Chen, M. Qiu, R. Wang, L. Zhang, C. Li, C. Ye, X. Zhou, *Bioconjugate Chem.* **2022**, *33*, 1729–1740.

[18] a) E. B. Adamson, K. D. Ludwig, D. G. Mummy, S. B. Fain, *Phys. Med. Biol.* **2017**, *62*, R81-R123; b) A. S. Khan, R. L. Harvey, J. R. Birchall, R. K. Irwin, P. Nikolaou, G. Schrank, K. Emami, A. Dummer, M. J. Barlow, B. M. Goodson, E. Y. Chekmenev, *Angew. Chem. Int. Ed.* **2021**, *60*, 22126–22147; c) L. L. Walkup, J. C. Woods, *NMR Biomed.* **2014**, *27*, 1429–1438.

[19] a) H. Li, X. Zhao, Y. Wang, X. Lou, S. Chen, H. Deng, L. Shi, J. Xie, D. Tang, J. Zhao, L. S. Bouchard, L. Xia, X. Zhou, *Sci. Adv.* **2021**, *7*, eabc8180; b) J. T. Grist, G. J. Collier, H. Walters, M. Kim, M. Chen, G. Abu Eid, A. Laws, V. Matthews, K. Jacob, S. Cross, A. Eves, M. Durrant, A. McIntyre, R. Thompson, R. F. Schulte, B. Raman, P. A. Robbins, J. M. Wild, E. Fraser, F. Gleeson, *Radiology* **2022**, *305*, 709–717; c) J. T. Grist, M. Chen, G. J. Collier, B. Raman, G. Abueid, A. McIntyre, V. Matthews, E. Fraser, L. P. Ho, J. M. Wild, F. Gleeson, *Radiology* **2021**, *301*, E353-E360.

[20] a) R. Yue, M. Zhou, X. Li, L. Xu, C. Lu, Z. Dong, L. Lei, H. Liu, G. Guan, Q. Liu, X. B. Zhang, G. Song, *ACS Nano* **2023**, *17*, 13792–13810; b) C. Zhang, L. Xu, B. Nan, C. Lu, H. Liu, L. Lei, R. Yue, G. Guan, M. He, X. B. Zhang, G. Song, *ACS Nano* **2023**, *17*, 9529–9542; c) C. Lu, Z. Li, N. Wu, D. Lu, X. Zhang, G. Song, *Chem* **2023**, *9*, 3185–3211.

[21] L. Dai, M. Yao, Z. Fu, X. Li, X. Zheng, S. Meng, Z. Yuan, K. Cai, H. Yang, Y. Zhao, *Nat. Commun.* **2022**, *13*, 2688.

[22] Y. Kaneda, *Adv. Drug Delivery Rev.* **2000**, *43*, 197–205.

[23] a) W. Chen, S. Li, C. Chen, L. Yan, *Adv. Mater.* **2011**, *23*, 5679–5683; b) M. Lu, H. Wu, D. Liu, F. Wang, Y. Wang, M. Wang, Q. Cui, H. Zhang, F. Zang, M. Ma, J. Ma, F. Shi, Y. Zhang, *ACS Nano* **2023**, *17*, 24170–24186.

[24] B. Li, T. Gong, N. Xu, F. Cui, B. Yuan, Q. Yuan, H. Sun, L. Wang, J. Liu, *Small* **2020**, *16*, e2003969.

[25] C. He, S. Wu, N. Zhao, C. Shi, E. Liu, J. Li, *ACS Nano* **2013**, *7*, 4459–4469.

[26] a) H. Dong, W. Du, J. Dong, R. Che, F. Kong, W. Cheng, M. Ma, N. Gu, Y. Zhang, *Nat. Commun.* **2022**, *13*, 5365; b) M. Zandieh, J. Liu, *Angew. Chem. Int. Ed.* **2022**, *61*, e202212013.

[27] R. Wang, M. Qiu, L. Zhang, M. Sui, L. Xiao, Q. Yu, C. Ye, S. Chen, X. Zhou, *Adv. Mater.* **2023**, *35*, e2306748.

[28] Q. Yu, L. Zhang, M. Jiang, L. Xiao, Y. Xiang, R. Wang, Z. Liu, R. Zhou, M. Yang, C. Li, M. Liu, X. Zhou, S. Chen, *Angew. Chem. Int. Ed.* **2023**, *62*, e202313137.
[29] R. Fan, C. Chen, M. Mu, D. Chuan, H. Liu, H. Hou, J. Huang, A. Tong, G. Guo, J. Xu, *ACS Nano* **2023**, *17*, 9126–9139.
[30] a) Q. Xue, D. Yan, X. Chen, X. Li, R. Kang, D. J. Klionsky, G. Kroemer, X. Chen, D. Tang, J. Liu, *Autophagy* **2023**, *19*, 1982–1996; b) W. S. Yang, R. SriRamaratnam, M. E. Welsch, K. Shimada, R. Skouta, V. S. Viswanathan, J. H. Cheah, P. A. Clemons, A. F. Shamji, C. B. Clish, L. M. Brown, A. W. Girotti, V. W. Cornish, S. L. Schreiber, B. R. Stockwell, *Cell* **2014**, *156*, 317–331.
[31] C. Yang, M. Wang, M. Chang, M. Yuan, W. Zhang, J. Tan, B. Ding, P. Ma, J. Lin, *J. Am. Chem. Soc.* **2023**, *145*, 7205–7217.
[32] a) H. Dong, Q. Li, Y. Zhang, M. Ding, Z. Teng, Y. Mou, *Adv. Sci.* **2023**, *10*, e2301339; b) S. K. Wculek, F. J. Cueto, A. M. Mujal, I. Melero, M. F. Krummel, D. Sancho, *Nat. Rev. Immunol.* **2020**, *20*, 7–24.
[33] J. P. Mugler 3rd, B. Driehuys, J. R. Brookeman, G. D. Cates, S. S. Berr, R. G. Bryant, T. M. Daniel, E. E. de Lange, J. H. Downs 3rd, C. J. Erickson, W. Happer, D. P. Hinton, N. F. Kassel, T. Maier, C. D. Phillips, B. T. Saam, K. L. Sauer, M. E. Wagshul, *Magn. Reson. Med.* **1997**, *37*, 809–915.

Manuscript received: February 22, 2024
Accepted manuscript online: March 29, 2024
Version of record online: ■■, ■■

Research Articles

Nanotheranostics

L. Zhang, M. Qiu, R. Wang, S. Li, X. Liu, Q. Xu, L. Xiao, Z.-X. Jiang, X. Zhou,* S. Chen* _____ e202403771

Monitoring ROS Responsive Fe_3O_4-based Nanoparticle Mediated Ferroptosis&Immunotherapy via ^{129}Xe MRI

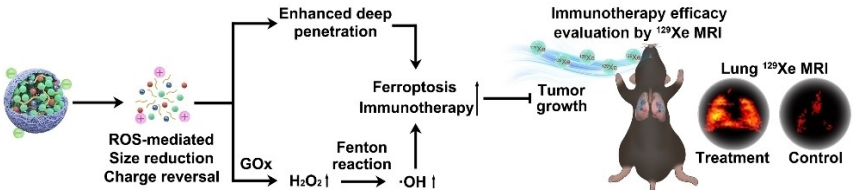

A self-supplying ROS-responsive Fe_3O_4 nanoparticle was designed to enhance the therapeutic efficacy of ferroptosis and immunotherapy by ROS-mediated size reduction and charge reversion. Moreover, the ^{129}Xe MRI of lung metastases showed significant differences in lung ventilation defects in the treatment and control groups, indicating the great potential of ^{129}Xe MRI for monitoring the immunotherapeutic efficacy of lung metastatic cancer.